

Parallel firehose instability in electron-positron plasmas

C.-S. Jao¹ and L.-N. Hau^{1,2,*}

¹*Institute of Space Science, National Central University, Taoyuan City, Taiwan, Republic of China*

²*Department of Physics, National Central University, Taoyuan City, Taiwan, Republic of China*

 (Received 19 December 2019; revised manuscript received 25 February 2020; accepted 13 March 2020; published 16 April 2020)

In a magnetized uniform plasma, firehose instability may arise as a result of pressure anisotropy of $P_{\parallel} > P_{\perp}$, where P_{\parallel} and P_{\perp} are the thermal pressure parallel and perpendicular to the magnetic field, respectively. In this paper, we examine the parallel firehose instability in electron-positron plasmas based on the particle simulations along with the linear fluid theory, which may give rise to the dispersion relation, instability criteria, and growth rate, etc., for comparisons with those calculated from the kinetic simulations. As for the firehose instability in electron-proton plasmas, the magnetic field grows rapidly and then decreases with oscillations. The nonlinear saturated state complies with the linear stability criterion, $\alpha = \mu_0(P_{\parallel} - P_{\perp})/B^2 = 1$, derived from the fluid theory only for relatively smaller values of initial α or ω_p/ω_c , where ω_p and ω_c are the plasma and cyclotron frequencies, respectively. For relatively larger values of initial α and ω_p/ω_c , the saturated α values are smaller than 1 as a result of kinetic resonant effects. The dominant wave numbers are $kc/\omega_p < 0.5$ and the growth rates are in the range of $0.1-0.3\omega_c$, which are approximately consistent with the linear fluid theory for the same wavelengths. Both electrostatic and electromagnetic modes predicted by the linear fluid theory are identified in the kinetic simulations.

DOI: [10.1103/PhysRevE.101.043205](https://doi.org/10.1103/PhysRevE.101.043205)

I. INTRODUCTION

In space and astrophysical plasma environments, temperature or pressure may tend to exhibit anisotropy due to the lack of sufficient collisions (see, e.g., Refs. [1,2]). In particular, in strongly magnetized plasmas, the pressure tensor can be described as the gyrotropic form with distinct P_{\parallel} and P_{\perp} , where P_{\parallel} and P_{\perp} are, respectively, the pressure components parallel and perpendicular to the magnetic field. The temperature anisotropy is a source of free energy for the development of firehose and mirror instabilities, etc. The firehose-type pressure anisotropy may easily develop as the solar or stellar wind expands outward with decreasing magnetic field as a result of the first adiabatic invariant [3]. For electron-proton plasmas, the studies of firehose instabilities have two categories, namely the proton and electron firehose instabilities, with the former being associated with the large-scale magnetic perturbations and the latter being associated with the electron acceleration observed in the solar wind and on the Sun (see, e.g., Refs. [3–5]). While the electron firehose with relatively short wavelengths is principally studied by kinetic models (see, e.g., Refs. [6,7]), the proton firehose may be studied based on the anisotropic magnetohydrodynamics (MHD)/Hall MHD or kinetic theory and simulations (see, e.g., Refs. [8–11]). Indeed, the well-known firehose instability criterion derived based on the linear gyrotropic MHD model [12] and linear Vlasov theory [13] has the same form of $\beta_{\parallel} - \beta_{\perp} > 2$.

The electron-positron plasma may be created in the presence of strong electromagnetic fields or under high temperatures via pair production. They have been found to exist

in the Earth's radiation belts and some astrophysical plasma environments such as the pulsar magnetosphere [14–19] as well as in laser plasma experiments [20–22]. An overall study of the electromagnetic waves in electron-positron plasmas with temperature anisotropy based on linear kinetic theory has confirmed the existence of firehose instability, which has the same instability criterion as the proton firehose instability [23]. Recently, there has been increasing interest in the study of nonlinear plasma instabilities driven by temperature anisotropy in electron-positron plasmas; for example, Dieckmann *et al.* [24] have examined the Weibel instability of pair plasmas and compared it with the results for electron plasmas for applications of laboratory and astrophysical systems such as the pulsar magnetosphere (see, e.g., Refs. [14,16]). In this study, we examine the firehose instability in electron-positron plasmas based on full particle simulations along with linear fluid theory. The present study will focus on the parallel propagation case for which the background magnetic field is aligned with the wave vector. In MHD theory with temperature anisotropy, the parallel proton firehose instability is associated with the incompressible Alfvén wave and may give rise to significant magnetic fluctuations [9–11]. Oblique proton firehose instabilities have also been shown to exist in electron-proton plasmas from both kinetic and anisotropic MHD theories, but the growth rates are generally not as significant as the parallel case (see, e.g., Ref. [25]). It is an interesting issue of whether significant magnetic field perturbations can also occur for the parallel firehose instability in electron-positron plasmas, which are in contrast to the electron-proton plasmas with distinct inertial asymmetry.

In this study, the evolution of collisionless firehose instabilities in electron-positron plasmas is examined based on particle simulations along with linear fluid theory that provides instability criteria and growth rate, etc. The intercomparisons

*lnhau@jupiter.ss.ncu.edu.tw

between the linear theory and kinetic simulations are made to infer the role of linear fluid theory in the nonlinear evolution of firehose instability. Note that we have recently shown that in electron-positron plasmas, the beam or streaming instability may also result in electromagnetic waves with magnetic field fluctuations resembling the firehose-type instability [26–28]. In particular, the particle simulations show that streaming electrons or positrons along the background magnetic field may first lead to electrostatic solitary waves and subsequently trigger the firehose-type instability as a result of parallel heating associated with the electrostatic structures [28]. In this study, the firehose instability is driven purely by pressure anisotropy in the background equilibrium.

II. LINEAR FLUID THEORY

In this section, the two-fluid models with anisotropic pressures together with the Maxwell equations shown in the following are adopted to obtain the dispersion relation and instability criteria for parallel firehose instability in electron-positron plasmas:

$$\frac{\partial n_j}{\partial t} + \nabla \cdot (n_j \bar{u}_j) = 0, \quad (1)$$

$$m_j \left[\frac{\partial n_j \bar{u}_j}{\partial t} + \nabla \cdot (n_j \bar{u}_j \bar{u}_j) \right] = -\nabla \cdot \vec{P}_j + n_j q_j \bar{E} + n_j q_j \bar{u}_j \times \vec{B}, \quad (2)$$

$$\nabla \times \bar{E} = -\frac{\partial \vec{B}}{\partial t}, \quad (3)$$

$$\nabla \times \vec{B} = \mu_o \sum_j n_j q_j \bar{u}_j + \frac{1}{c^2} \frac{\partial \bar{E}}{\partial t}. \quad (4)$$

In the above equations, m_j and q_j are the mass and electric charge of particles, respectively. The quantities n_j , \vec{P}_j , and \bar{u}_j are the number density, thermal pressure, and drift velocity of fluids, respectively. The subscript j denotes two different components, i.e., electrons and positrons, in the plasma system. The thermal pressures in Eq. (2) have the gyrotropic form $\vec{P} = P_{\perp} \bar{1} + (P_{\parallel} - P_{\perp}) \vec{B} \vec{B} / B^2$, with two components, P_{\parallel} and P_{\perp} , which need be described by a set of energy laws, say, the double-adiabatic laws or the more generalized energy closures such as the double-polytropic laws [29,30]. Note that the relativistic effects may enter the problem as the thermal speeds of charged particles are comparable to the speed of light which might occur in certain high-energy astrophysical environments. In the following analyses, the ratios of thermal speed to the speed of light are about 1/32–3/8 so that the Lorentz factors are close to 1 when considering the relativistic effects. For ultrarelativistic anisotropic plasmas, the dispersion relations for linear MHD waves and instabilities may be found in the paper by Chou and Hau [31] while the corresponding relations for two-component plasmas are still lacking.

In this study, we consider the parallel propagation case in which the electrostatic (ES) and electromagnetic (EM) modes become decoupled. The ES mode is compressible with no perturbations in the magnetic field and perpendicular pressure,

and the density and parallel pressure may follow the adiabatic law, $P_{\parallel} = C n^{\gamma}$. The EM modes are incompressible with no density and pressure perturbations, and thus they are not affected by the forms of energy closures. Linearization of the above equations yields

$$-i\omega \delta n_j + i n_{0,j} \bar{k} \cdot \delta \bar{u}_j = 0, \quad (5)$$

$$m_j n_{0,j} (-i\omega \delta \bar{u}_j) = -i(\delta P_{\perp,j} \bar{k} + k \alpha_{0,j} B_0 \delta \bar{B} / \mu_o + k \delta \alpha_j B_0 \bar{B}_0 / \mu_o) + n_{0,j} q_j \delta \bar{E} + n_{0,j} q_j \delta \bar{u}_j \times \vec{B}_0, \quad (6)$$

$$i \bar{k} \times \delta \bar{E} = i\omega \delta \vec{B}, \quad (7)$$

$$i \bar{k} \times \delta \vec{B} = \mu_o \sum_j n_{0,j} q_j \delta \bar{u}_j + i\omega \delta \bar{E} / c^2, \quad (8)$$

for which $\alpha_{0,j} = \mu_o (P_{\parallel,0,j} - P_{\perp,0,j}) / B_0^2$ and $\delta \alpha_j = \mu_o (\delta P_{\parallel,j} - \delta P_{\perp,j}) / B_0^2$. For the ES mode, $\delta \vec{B} = 0$ while for the EM mode, $\delta P_{\perp,j} = \delta P_{\parallel,j} = 0$. The dispersion relations are obtained by eliminating $\delta \bar{u}_j$ from Eqs. (5)–(7) in Eq. (8), which for $\bar{k} \parallel \vec{B}_0$ may be separated into the ES (longitudinal) and EM (transverse) modes.

In the following studies, both electrons and positrons in the system are assumed to have the same equilibrium number density, $n_0/2$, perpendicular thermal pressure, $P_{\perp,0}/2$, and parallel thermal pressure, $P_{\parallel,0}/2$. The dispersion relations of the longitudinal mode and the transverse mode are, respectively,

$$1 = \frac{\omega_p^2}{\omega^2 - k^2 c_{S,\parallel}^2}, \quad (9)$$

$$\frac{\omega^2}{c^2 k^2} = \frac{\omega^2 - (1 - \alpha_0) \omega_c^2}{\omega^2 - \omega_c^2 - \omega_p^2}, \quad (10)$$

for which $c_{S,\parallel}^2 \equiv \gamma_{\parallel} P_{\parallel,0} / m n_0$, $\omega_p^2 \equiv n_0 e^2 / m \epsilon_0$, and $\omega_c \equiv e B_0 / m$. Also note that the thermal pressures $P_{\parallel,0}$ and $P_{\perp,0}$ in the system are the total pressures, $P_{\parallel,0} = P_{\parallel,0,e} + P_{\parallel,0,p}$ and $P_{\perp,0} = P_{\perp,0,e} + P_{\perp,0,p}$, where the subscripts e and p denote the electron and positron components, respectively. The longitudinal mode shown in Eq. (9) is the electrostatic Langmuir mode of pair plasmas, which will also be identified in the kinetic simulations. As expected for the parallel propagation case, the dispersion relation of the transverse mode (10) is independent of the energy closure, and the L and R modes are indistinguishable for the pair plasma system [32,33]. The four roots for the transverse mode are as follows:

$$\omega_{1,2}^2 = \frac{1}{2} [\omega_p^2 + \omega_c^2 + c^2 k^2 + \sqrt{(\omega_p^2 + \omega_c^2 + c^2 k^2)^2 - 4c^2 k^2 \omega_c^2 (1 - \alpha_0)}], \quad (11)$$

$$\omega_{3,4}^2 = \frac{1}{2} [\omega_p^2 + \omega_c^2 + c^2 k^2 - \sqrt{(\omega_p^2 + \omega_c^2 + c^2 k^2)^2 - 4c^2 k^2 \omega_c^2 (1 - \alpha_0)}], \quad (12)$$

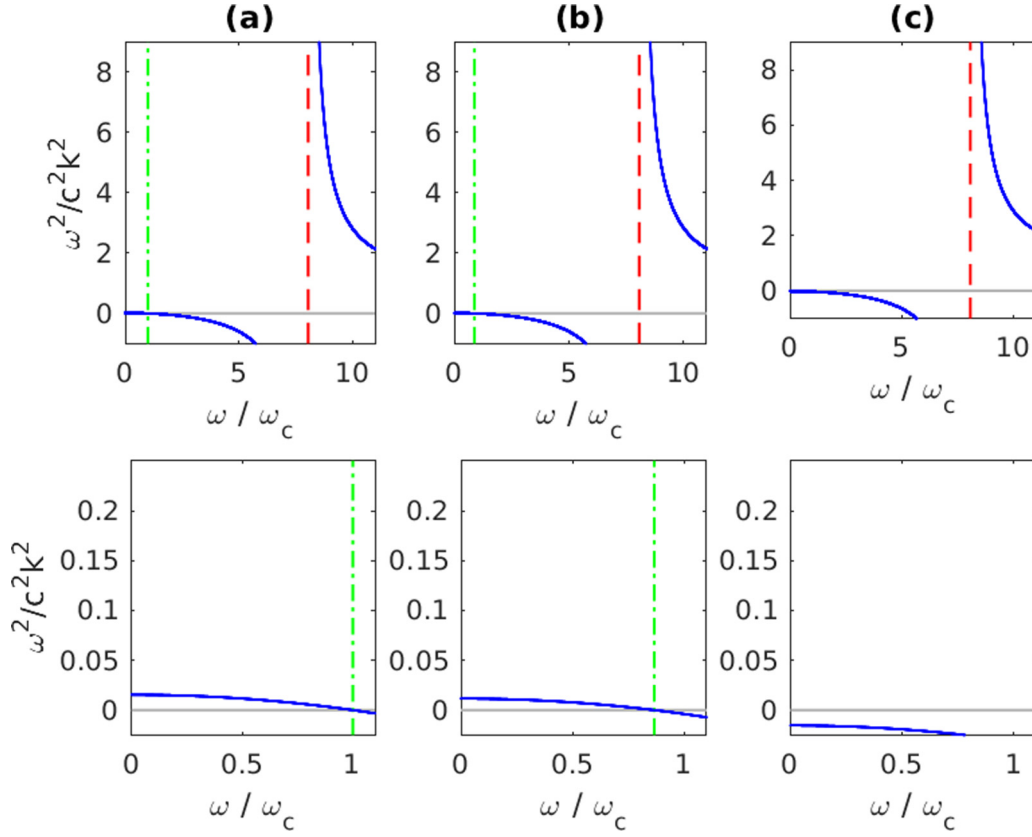


FIG. 1. The phase velocity ω^2/c^2k^2 of the transverse mode vs wave frequency with $\omega_p/\omega_c = 8$ and (a) $\alpha_0 = 0$, (b) $\alpha_0 = 0.25$, and (c) $\alpha_0 = 2.0$. The dashed and dot-dashed lines in each panel denote the cutoff frequency $\omega_{\text{cut}} = \sqrt{\omega_c^2 + \omega_p^2}$ and the resonance frequency $\omega_{\text{res}} = \sqrt{1 - \alpha_0}\omega_c$, respectively. The bottom panels are the low-frequency parts of the top panels.

where $\omega_{1,2}$ and $\omega_{3,4}$ correspond to the upper and lower frequency branches, respectively. The instability criteria derived from Eqs. (11) and (12) are, respectively,

$$\beta_{\perp,0} - \beta_{\parallel,0} > \frac{(\omega_p^2 + \omega_c^2 + c^2k^2)^2}{2c^2k^2\omega_c^2} - 2, \quad (13)$$

$$\beta_{\parallel,0} - \beta_{\perp,0} > 2, \quad (14)$$

where $\beta_{\parallel,0} = P_{\parallel,0}/(B_0^2/\mu_0)$ and $\beta_{\perp,0} = P_{\perp,0}/(B_0^2/\mu_0)$. Equations (13) and (14) are the criteria for cyclotron instability ($P_{\perp,0} > P_{\parallel,0}$) and firehose instability ($P_{\parallel,0} > P_{\perp,0}$), respectively. For cyclotron instability, all four roots are complex numbers with real and imaginary parts implying that the cyclotron mode is a propagating instability. For firehose instability, $\omega_{1,2}$ are real and $\omega_{3,4}$ are purely imaginary so it is a purely growing mode. Note that the firehose instability criterion (14), commonly written as $\alpha_0 > 1$, is consistent with the result based on the kinetic theory [23]. In the following, we show the growth rate calculations for various parameter values that are not addressed in the prior study of kinetic firehose instability in pair plasmas [23].

Figure 1 shows the phase velocity v_ϕ^2/c^2 of the transverse mode versus wave frequency in Eq. (10). The dashed and dot-dashed lines in the figure denote the cutoff frequency $\omega_{\text{cut}} = \sqrt{\omega_c^2 + \omega_p^2}$ and the resonance frequency $\omega_{\text{res}} = \sqrt{1 - \alpha_0}\omega_c$, respectively, derived from Eq. (10). For the isotropic case ($\alpha_0 = 0$) shown in panel (a), the transverse

mode may propagate in the frequency regime less than the resonance frequency ω_c or larger than the cutoff frequency $\sqrt{\omega_c^2 + \omega_p^2}$. We may separate the transverse mode into lower and upper frequency branches based on this property [32,33]. For $P_{\parallel,0} > P_{\perp,0}$ but $\alpha_0 < 1$ shown in panel (b), ω_{res} decreases with increasing α_0 value, implying the narrower propagation regime for the lower frequency branch. On the other hand, the upper frequency branch maintains stable propagation above the cutoff frequency $\sqrt{\omega_c^2 + \omega_p^2}$, while for $\alpha_0 > 1$ [panel (c)] ω_{res} no longer exists and only the upper frequency branch may propagate in the system.

Figure 2 shows the wave frequency versus wave number of the transverse mode for the cases with $\alpha_0 = 0$ [panel (a)], $\alpha_0 = 0.25$ [panel (b)], and $\alpha_0 = 2.0$ [panel (c)]. The solid and dashed curves in all panels denote the real and imaginary parts of the wave frequency, respectively, derived from Eqs. (11) and (12). For the isotropic case [$\alpha_0 = 0$, panel (a)] and the modest anisotropic case [$\alpha_0 = 0.25$, panel (b)], as in Fig. 1, the upper frequency branch can only propagate with frequency higher than $\omega_{\text{cut}} = 2.23\omega_c$ and the lower frequency branch may propagate with frequency lower than ω_{res} . For $\alpha_0 > 1$ [panel (c)], the lower frequency branch becomes a purely growing unstable mode.

Figure 3 shows the linear growth rate of the firehose mode as functions of wave number and α_0 values. As expected, the linear growth rate generally increases with increasing α_0 values. The growth rate also mostly increases with increasing

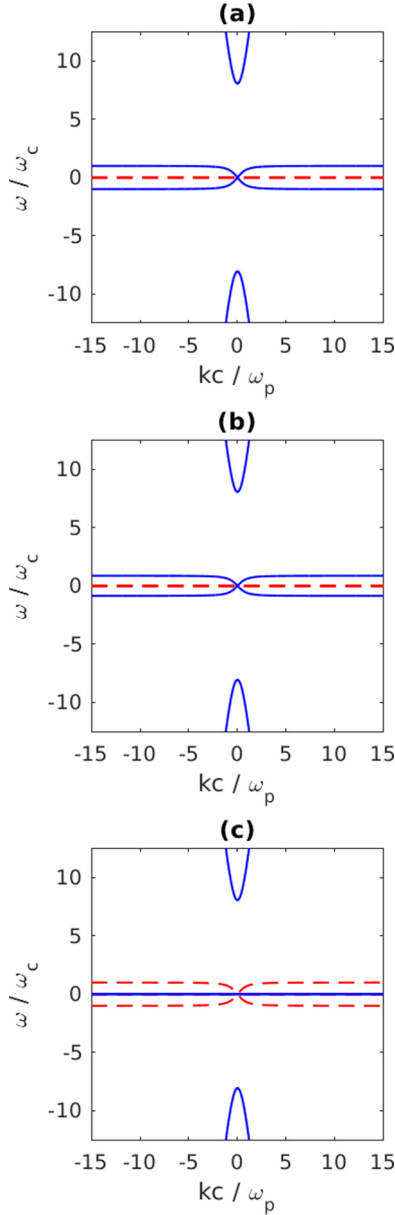


FIG. 2. The wave frequency vs wave number of the transverse mode with $\omega_p/\omega_c = 8$ and (a) $\alpha_0 = 0$, (b) $\alpha_0 = 0.25$, and (c) $\alpha_0 = 2.0$. The solid and dashed curves in each panel denote the real part ω_r and the imaginary part ω_i of the wave frequency, respectively.

k and approaches a nearly constant value for $kc/\omega_p > 1$ or $\lambda < \lambda_{sd} = c/\omega_p$. Note that λ_{sd} is the characteristic length of the electron and positron fluid model, thus the physics may not be definable for $\lambda < \lambda_{sd}$. Figure 4 shows the saturated growth rate of the firehose instability as functions of ω_p/ω_c and α_0 values, indicating that the saturated growth rate may reach $\sim 1.75\omega_c$ and is independent of the varying ω_p/ω_c values.

As shown in Eq. (14), the instability criterion of the firehose instability seems to be the same for both electron-positron and electron-proton plasmas. The fluid models adopted for both plasma systems, however, are not the same; in particular, the two-fluid model with pressure anisotropy is adopted for electron-positron plasmas, while the ideal anisotropic MHD model is used to derive the criterion of

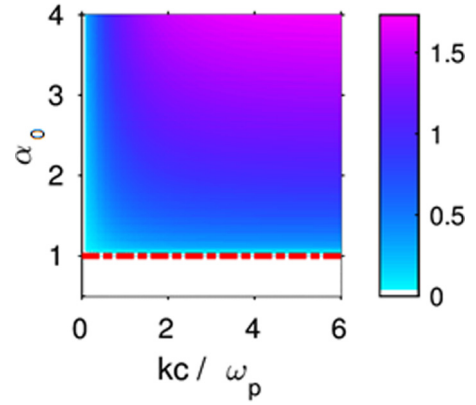


FIG. 3. The imaginary part of the wave frequency ω_i/ω_c of the transverse mode as functions of the wave number and α_0 value with $\omega_p/\omega_c = 8$. The dot-dashed curve in the figure denotes the firehose instability threshold.

$\alpha_0 > 1$ for proton firehose instability. In the ideal MHD model with pressure anisotropy, the frozen-in-flux condition $\vec{E} + \vec{u} \times \vec{B} = 0$ is assumed, which is the mechanism for the growth of the magnetic field perturbations. The two-fluid equations shown above may in principle be combined into one-fluid equations along with the generalized Ohm's law, and the ideal MHD model is the result of neglecting the inertial effects in the generalized Ohm's law in the one-fluid formulation. It is interesting to derive the corresponding generalized Ohm's law for the parallel firehose instability in electron-positron plasmas. In particular, the following modified frozen-in-flux condition is obtained from the linearized electron-positron fluid equations:

$$\delta \vec{E} + \delta \vec{u} \times \vec{B}_0 \left(\frac{\omega_c^2 - \omega^2}{\omega_c^2} \right) \left(\frac{1}{1 + \alpha_0 k^2 \lambda_{sd}^2} \right) = \vec{0}, \quad (15)$$

where $\delta \vec{u} = (n_{0,e} \delta \vec{u}_e + n_{0,p} \delta \vec{u}_p) / (n_{0,e} + n_{0,p})$. For low-frequency and long-wavelength limits, $\omega \ll \omega_c$ and $\alpha_0 k^2 \lambda_{sd}^2 \ll 1$, Eq. (15) becomes $\delta \vec{E} + \delta \vec{u} \times \vec{B}_0 = 0$, complying with the frozen-in-flux condition. The modified frozen-flux condition will be examined in the particle simulations.

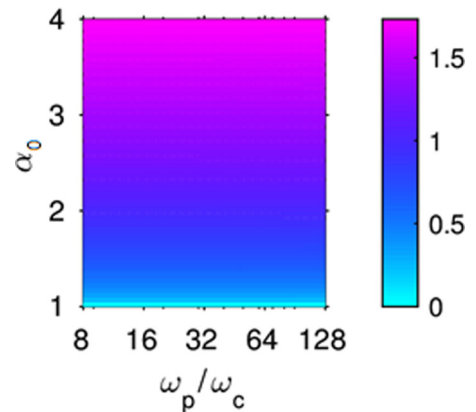


FIG. 4. The saturated growth rate of the firehose instability as functions of ω_p/ω_c and α_0 values.

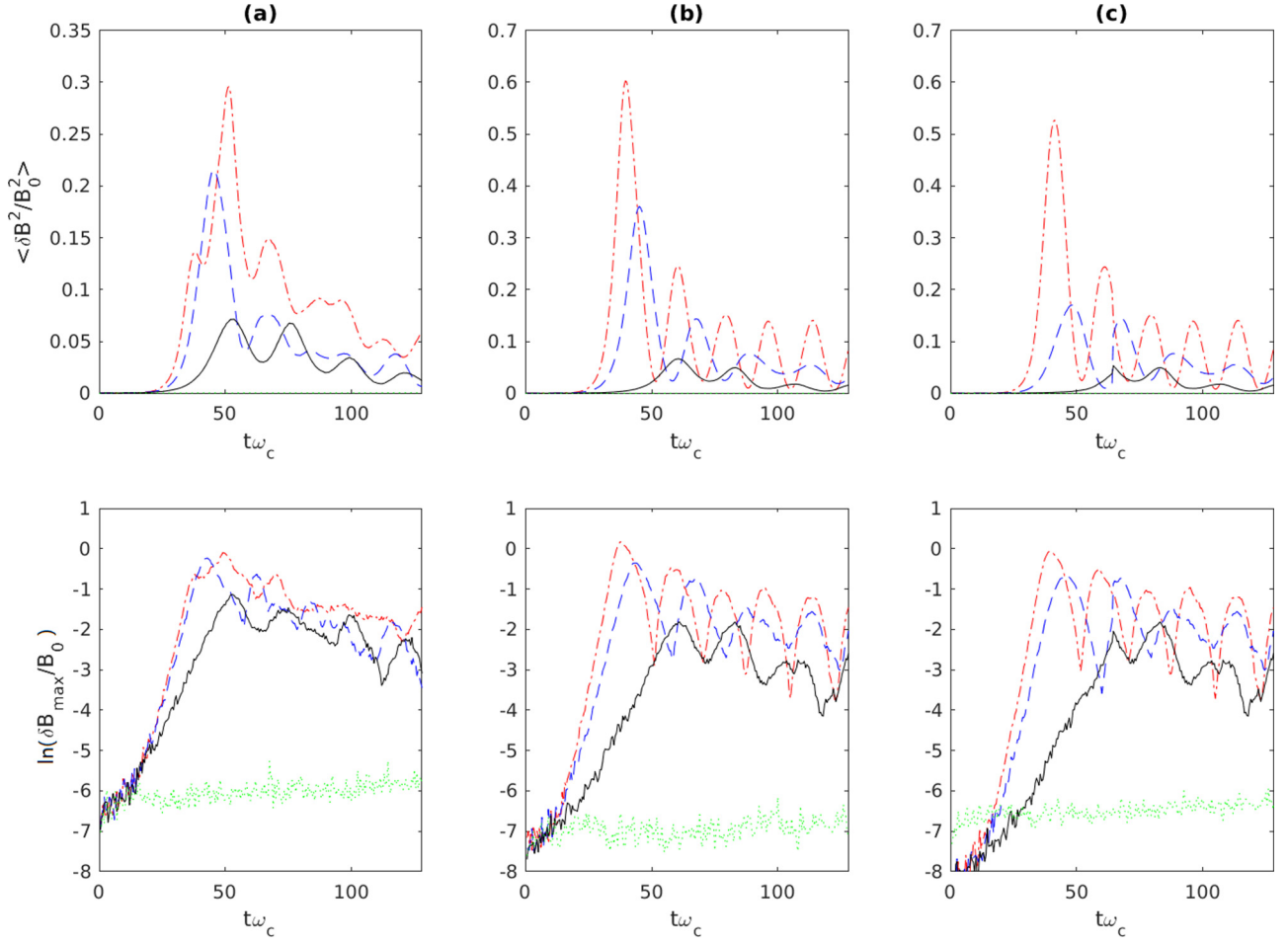


FIG. 5. Time evolution of the average perturbed magnetic field $\langle \delta B^2 / B_0^2 \rangle$ (top panels) and maximum perturbed magnetic field $\delta B_{\max} / B_0$ (bottom panels) for the cases with $\beta_{\parallel,0} = 10$, $\beta_{\perp,0} = 2$ ($\alpha_0 = 4$, dot-dashed curve), $\beta_{\parallel,0} = 8$, $\beta_{\perp,0} = 2$ ($\alpha_0 = 3$, dashed curve), $\beta_{\parallel,0} = 6$, $\beta_{\perp,0} = 2$ ($\alpha_0 = 2$, solid curve), and $\beta_{\parallel,0} = 4$, $\beta_{\perp,0} = 2$ ($\alpha_0 = 1$, dotted curve) and with (a) $\omega_p/\omega_c = 32$, (b) $\omega_p/\omega_c = 16$, and (c) $\omega_p/\omega_c = 8$ based on the kinetic simulations.

Nonlinear simulations

The fluid model used for the linear analyses contains no transport effects and thus is not suitable for examining the nonlinear evolution of collisionless firehose instabilities. In this section, we show the calculation results from a one-dimensional electromagnetic particle simulation model that is developed largely based on the published particle-in-cell model, KEMPO1 [34,35]. In particular, the Buneman-Boris method is used to solve the relativistic equations of motion, while the leap-frog scheme along with the standard second-order central difference method is applied to solving the Faraday and Ampère laws for the magnetic and electric fields, respectively. The current density on the grids is calculated by taking all the particles in the neighboring cells based on the linear interpolation weight. The numerical model was benchmarked and applied recently to the study of streaming instability in electron-positron plasmas [28]. In the calculations, dimensionless units with $v_{\text{th},\perp} = 1.0$ (the thermal velocity perpendicular to the background magnetic field) and $\omega_p = 1.0$ are used. The time interval $\Delta t = 0.01\omega_p^{-1}$ and the grid size $\Delta x = 1\lambda_D$ ($\lambda_D = v_{\text{th},\perp}\omega_p^{-1}$) are set for all cases. The number density of both electrons and positrons is 128 pairs

per cell. Note that we have carried out the experiments with various particle numbers (64, 128, and 256 pairs per cell) and confirmed that the results are essentially the same. The boundary of the simulation system is periodic, and the length

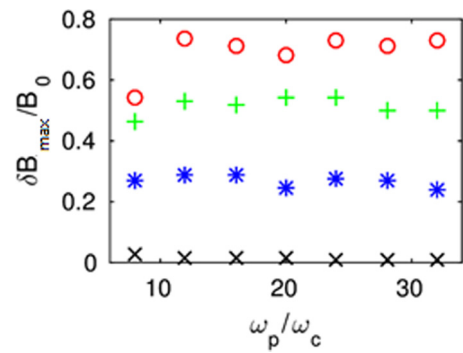


FIG. 6. The maximum perturbed magnetic field $\delta B_{\max} / B_0$ vs frequency ratio ω_p / ω_c for the cases with $\beta_{\parallel,0} = 10$, $\beta_{\perp,0} = 2$ ($\alpha_0 = 4$, circle symbols), $\beta_{\parallel,0} = 8$, $\beta_{\perp,0} = 2$ ($\alpha_0 = 3$, plus symbols), $\beta_{\parallel,0} = 6$, $\beta_{\perp,0} = 2$ ($\alpha_0 = 2$, star symbols), and $\beta_{\parallel,0} = 4$, $\beta_{\perp,0} = 2$ ($\alpha_0 = 1$, cross symbols).

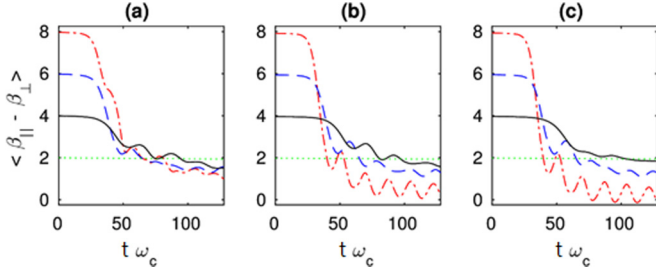


FIG. 7. Time evolution of the average $\langle \beta_{\parallel} - \beta_{\perp} \rangle$ value for the cases with $\beta_{\parallel,0} = 10, \beta_{\perp,0} = 2$ ($\alpha_0 = 4$, dot-dashed curve); $\beta_{\parallel,0} = 8, \beta_{\perp,0} = 2$ ($\alpha_0 = 3$, dashed curve); $\beta_{\parallel,0} = 6, \beta_{\perp,0} = 2$ ($\alpha_0 = 2$, solid curve); and $\beta_{\parallel,0} = 4, \beta_{\perp,0} = 2$ ($\alpha_0 = 1$, dotted curve) and with (a) $\omega_p/\omega_c = 32$, (b) $\omega_p/\omega_c = 16$, and (c) $\omega_p/\omega_c = 8$.

of the simulation domain is kept as $L = 64c/\omega_p$. The background magnetic field is along the x direction, and the initial particle velocity of both species is described by the bi-Maxwellian distribution. In all cases, $\beta_{\perp,0} = 2$ and $\beta_{\parallel,0} = 4-10$ and the frequency ratios $\omega_p/\omega_c = 8-32$ are chosen for comparison with the linear fluid theory. Note that recently there have been several studies on electron firehose instability with bi-kappa functions as the initial velocity distribution (see, e.g., Refs. [36,37]). The present study can in principle be extended to more general cases with the initial kappa velocity distribution, which introduces another free parameter in the simulation model.

Figure 5 shows the time evolution of the average perturbed magnetic field $\langle \delta B^2/B_0^2 \rangle$ (top panels) and the maximum perturbed magnetic field $\delta B_{\max}/B_0$ (bottom panels) for the cases with various values of $\beta_{\parallel,0}$ and the frequency

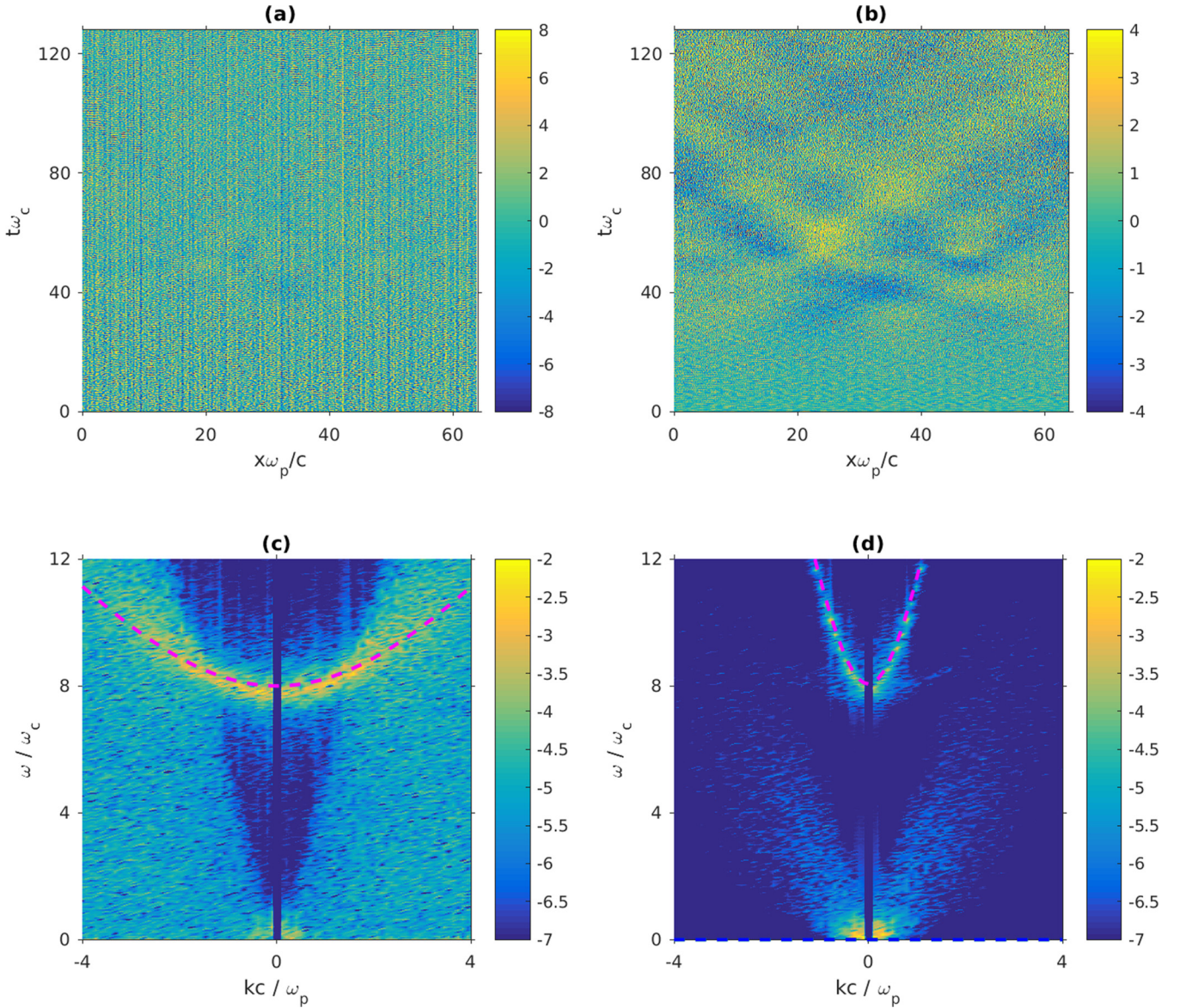


FIG. 8. Spatial and temporal evolution of (a) $E_x(x, t)$ and (b) $E_y(x, t)$ and the Fourier spectrum of (c) $E_x(k, \omega)$ and (d) $E_y(k, \omega)$ for the case with $\beta_{\parallel,0} = 8, \beta_{\perp,0} = 2$, and $\omega_p/\omega_c = 8$. The dashed curves in the bottom panels are the dispersion relations of the longitudinal mode [in panel (c)] and the transverse mode [in panel (d)] from the linear theory.

ratios ω_p/ω_c . According to the firehose instability criterion $\beta_{\parallel,0} - \beta_{\perp,0} > 2$ predicted from the fluid theory, the cases with $\beta_{\parallel,0} = 10$, $\beta_{\perp,0} = 2$ ($\alpha_0 = 4$, dot-dashed curve), $\beta_{\parallel,0} = 8$, $\beta_{\perp,0} = 2$ ($\alpha_0 = 3$, dashed curve), and $\beta_{\parallel,0} = 6$, $\beta_{\perp,0} = 2$ ($\alpha_0 = 2$, solid curve) are unstable, while the case with $\beta_{\parallel,0} = 4$, $\beta_{\perp,0} = 2$ ($\alpha_0 = 1$, dotted curve) is marginally stable. As shown in the figures, there is no obvious magnetic fluctuation for the case with $\beta_{\parallel,0} = 4$, $\beta_{\perp,0} = 2$ (dotted curve). As for the unstable cases, in the early stage, the maximum magnetic field fluctuations can grow up to $\delta B_{\max}/B_0 \sim 0.75$ in the case with $\beta_{\parallel,0} = 10$, $\beta_{\perp,0} = 2$, and $\omega_p/\omega_c > 8$. As expected, the initial growth rate increases with increasing α_0 and the linear growth rates in particle simulations are in the range of 0.1–0.3 ω_c in contrast to the maximum growth rates of 0.5–1.75 ω_c for $kc/\omega_p > 1$ (or $\lambda < 6.3 c/\omega_p$) as predicted by linear fluid theory. We will discuss this discrepancy further in the following. After the peaks that occur at $t\omega_c \sim 50$ for all unstable cases, the magnetic field exhibits oscillatory features that are similar to the nonlinear evolution process of the firehose instabilities in electron-proton plasmas (see, e.g., Refs. [7–10]). The oscillation periods are independent of ω_p/ω_c but slightly shorter with increasing $\beta_{\parallel,0}$ value (i.e., α_0). The quantity $\delta B_{\max}/B_0$ with various values of $\beta_{\parallel,0}$ and ω_p/ω_c is shown in Fig. 6, which shows that the maximum amplitude of magnetic perturbations increases with increasing α_0 but is nearly independent of ω_p/ω_c .

Figure 7 shows the time evolution of the average $\langle \beta_{\parallel} - \beta_{\perp} \rangle$ value in the nonlinear calculations. Note that the particle velocity distributions in all cases are the bi-Maxwellian distribution initially, and the root-mean-square velocity of particles is used to infer the thermal pressure as well as the corresponding β values in nonlinear calculations. For all unstable cases, the average $\langle \beta_{\parallel} - \beta_{\perp} \rangle$ values decrease sharply after $t\omega_c \sim 50$ and reach $\langle \beta_{\parallel} - \beta_{\perp} \rangle \leq 2$ in the final stage. The oscillatory features are associated with the magnetic field perturbations, which are decreased after $t\omega_c \sim 50$. As shown, only for relatively smaller α_0 and ω_p/ω_c values does the nonlinear evolution comply with the quasilinear fluid theory with $\alpha_0 = 1$ at the saturated state. For the cases with relatively larger α_0 or ω_p/ω_c values, the saturated states have smaller α values, a result also seen in proton firehose instability [10].

Figure 8 shows the temporal and spatial evolution of electric field for the case with $\beta_{\parallel,0} = 8$, $\beta_{\perp,0} = 2$, and $\omega_p/\omega_c = 8$. For the longitudinal mode [panel (a)], the amplitude of longitudinal fluctuations $E_x(x, t)$ remains the same as that of the initial phase. The corresponding Fourier spectrum $E_x(k, \omega)$ for the time interval of $t\omega_c = 0$ –128 is shown in Fig. 8(c). As indicated, the Langmuir mode can be observed and described by the linear dispersion relation shown in Eq. (9) [dashed curves in Fig. 8(c)]. As for the electric field [Fig. 8(b)], $E_y(x, t)$ starts to grow after $t\omega_c = 35$ and reaches the same order as the longitudinal mode $E_x(x, t)$, which is associated with the growing magnetic field fluctuations shown in Fig. 5(a) (dot-dashed curve). In the Fourier spectrum $E_y(k, \omega)$ shown in Fig. 8(d), the perturbation in the higher-frequency branch, corresponding to the transverse mode dispersion relation shown in Eq. (10), is observed, which is a stably propagating mode in the frequency range higher than $\omega_{\text{cut}} = \sqrt{\omega_c^2 + \omega_p^2}$. On the other hand, apparent perturbations are also present in the low-

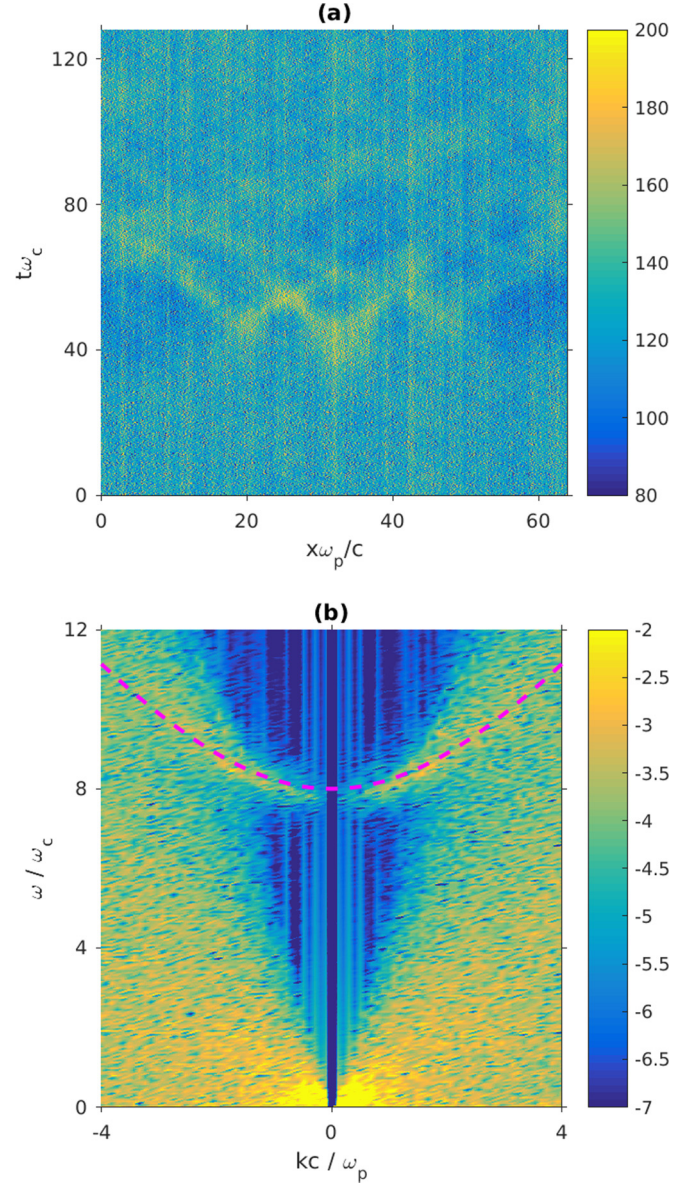


FIG. 9. Spatial and temporal evolution of the positron density $n_p(x, t)$ [panel (a)] and the corresponding Fourier spectrum $n_p(k, \omega)$ [panel (b)] for the case with $\beta_{\parallel,0} = 8$, $\beta_{\perp,0} = 2$, and $\omega_p/\omega_c = 8$. The dashed curve in the bottom panel is the dispersion relation of the longitudinal mode from the linear theory.

frequency and small-wave-number regime, which are related to the predicted nonpropagation unstable mode.

Figure 9 shows the temporal and spatial evolutions (top panels) and the corresponding Fourier spectrum (bottom panels) of positron number density for the same case ($\beta_{\parallel,0} = 8$, $\beta_{\perp,0} = 2$, and $\omega_p/\omega_c = 8$). As indicated, there exist density fluctuations of short and/or long wavelengths throughout the course of nonlinear evolution. The Fourier spectrum (bottom panel) further indicates that the density perturbations are present in both the high- and low-frequency regimes. The short-wavelength or high-frequency parts are associated with the linear Langmuir mode, while the long-wavelength or low-frequency perturbations developing in the later phase appear to be due to the nonlinear effects.

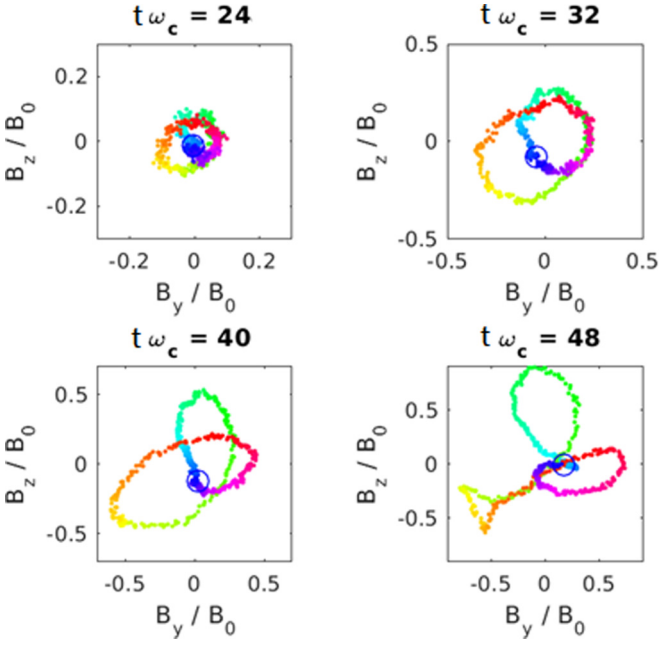


FIG. 10. The magnetic field hodograms for the spatial domain of $x = 0-512c/\omega_p$ for the case with $\beta_{\parallel,0} = 8$, $\beta_{\perp,0} = 2$, and $\omega_p/\omega_c = 8$. The circle symbol in each panel denotes the value of (B_y, B_z) at $x = 0$. From $x = 0$ to $512c/\omega_p$, the color is changing from blue, green, yellow, orange, red, magenta, and back to blue.

The magnetic field hodograms for the same case at various times ($t\omega_c = 24, 32, 40$, and 48) are shown in Fig. 10. As indicated, both B_y and B_z are comparable and the magnetic field can possess left-handed polarization ($t\omega_c = 24, 32, 40$) or mixed left-handed and right-handed polarizations toward the saturated state ($t\omega_c = 48$). According to the linear fluid theory, the electromagnetic or transverse modes have no distinguishable right-handed and left-handed polarization in electron-positron plasmas with the same parameter values. It is thus possible to observe both magnetic field polarizations in the same nonlinear simulations.

As shown in Fig. 8(d) for $\beta_{\parallel,0} = 8$, $\beta_{\perp,0} = 2$, and $\omega_p/\omega_c = 8$, the perturbations in the lower frequency branch are pronounced only in the regime of $kc/\omega_p < 0.5$ (or $\lambda > 12.5 c/\omega_p$). The average growth rate for $t\omega_c = 20-40$ is $0.25 \omega_c$ for the dominant wavelength ($kc/\omega_p = 0.29$ or $\lambda = 21.3 c/\omega_p$), which is slightly smaller than the value of $0.37\omega_c$ predicted by linear fluid theory for the same wavelength. Note that in accordance with the linear fluid theory, the maximum growth rate is $1.5\omega_c$ for $kc/\omega_p > 1$ (or $\lambda < 6.3c/\omega_p$), while in the kinetic simulations the perturbations for $kc/\omega_p > 1$ exist only for the longitudinal mode but are nearly absent for the transverse mode even in the early phase of time evolution. This is likely attributed to the limitations of the fluid theory in describing the physics of the electromagnetic modes for $\lambda < c/\omega_p$. The dominance of longer wavelength modes in the kinetic simulations may further be illustrated by checking the modified frozen-in-flux condition in the calculations. In particular, as shown in Eq. (15), for long-wavelength modes $\alpha_0 k^2 \lambda_{sd}^2 \ll 1$, the frozen-in-flux condition is more valid. Figure 11 shows the spatial distributions of $\delta \vec{E}/B_0$ (dot sym-

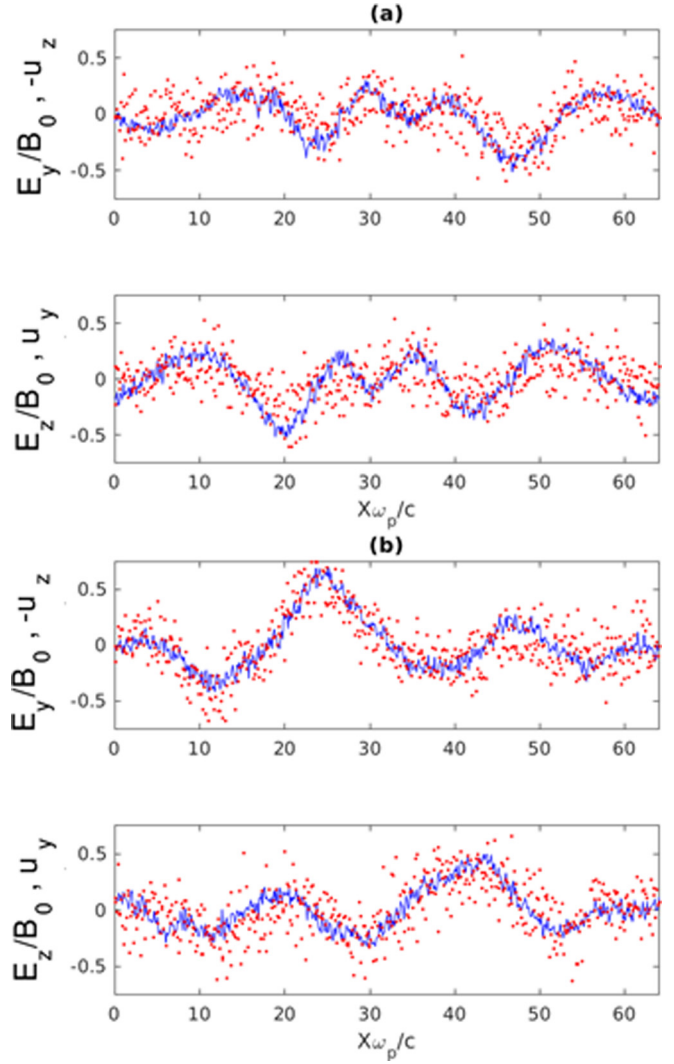


FIG. 11. The spatial distributions of $\delta \vec{E}/B_0$ (red dot symbols) and $\delta \vec{u}$ (blue solid curve) for the case with $\beta_{\parallel,0} = 8$, $\beta_{\perp,0} = 2$, and $\omega_p/\omega_c = 8$ at (a) $t\omega_c = 48$ and (b) $t\omega_c = 60$.

bols) and $\delta \vec{u}$ (solid curve) before and after the occurrence of maximum magnetic field perturbation for the case with $\beta_{\parallel,0} = 8$, $\beta_{\perp,0} = 2$, and $\omega_p/\omega_c = 8$. As indicated, the component $\delta E_y/B_0$ ($\delta E_z/B_0$) can be fitted well with the quantity $-\delta u_z$ (δu_y) in the large-scale limit, implying the validity of $\delta \vec{E} + \delta \vec{u} \times \vec{B}_0 \sim 0$ for small wave number approximation as predicted by linear fluid theory. The growth of significant magnetic field perturbations is apparently attributed to the long-wavelength modes in nonlinear kinetic simulations which, however, does not imply that the one-fluid MHD model with temperature anisotropy is suitable for describing the electron-positron firehose instability. In particular, as shown in Fig. 11, the $\vec{E} \times \vec{B}$ drift has a wide range as compared to the simple velocity profile.

III. CONCLUSIONS

In this paper, we have examined the firehose instability in electron-positron plasmas based on linear fluid theory and

full particle simulations. As for the parallel firehose instability in electron-proton plasmas, the instability occurs for $\beta_{\parallel} - \beta_{\perp} > 2$ and is a purely growing mode. In the kinetic simulations, the saturated state agrees with the fluid threshold only for relatively smaller pressure anisotropy and stronger magnetic field. For large temperature anisotropy and weak magnetic field, the saturated state has $\beta_{\parallel} - \beta_{\perp} < 2$, which is due to the kinetic resonant effects and is also seen in the hybrid simulation of firehose instability in electron-proton plasmas. In the nonlinear simulation, the magnetic field increases rapidly in the initial stage, reaching a peak value, and then decreases with oscillations. These features resemble the proton firehose instabilities developing in the fluid and kinetic simulations. The growth rate and the dominant wave number of firehose instability in the particle simulations, however, are smaller than the predicted values based on linear fluid theory as a result of kinetic effects. Nevertheless, all the wave modes

including the longitudinal electrostatic mode and the transverse electromagnetic modes predicted by the fluid theory are identified in the kinetic simulations. We have also derived the modified frozen-in-flux condition for the electron-positron firehose instability, and we examined the relation in kinetic simulations. It is shown that the frozen-in-flux condition approximately holds for the dominant long-wavelength scales, which may contribute to the growth of large-scale magnetic field perturbations in electron-positron plasmas.

ACKNOWLEDGMENTS

This research is supported by the Ministry of Science and Technology of the Republic of China (Taiwan) under Grants No. MOST107-2111-M-008-029-MY2, No. MOST108-2811-M-008-532, and No. MOST108-2111-M-008-044 to National Central University.

-
- [1] J. C. Kasper, A. J. Lazarus, and S. P. Gary, *Geophys. Res. Lett.* **29**, 20-1 (2002).
 - [2] M. Federico and A. S. Alexander, *Mon. Not. R. Astron. Soc.* **440**, 3226 (2014).
 - [3] L. Matteini, S. Landi, P. Hellinger, F. Pantellini, M. Maksimovic, M. Velli, B. E. Goldstein, and E. Marsch, *Geophys. Res. Lett.* **34**, L20105 (2007).
 - [4] S. P. Gary, R. M. Skoug, J. T. Steinberg, and C. W. Smith, *Geophys. Res. Lett.* **28**, 2759 (2001).
 - [5] O. A. Benz and P. Saint-Hilaire, *Adv. Space Res.* **32**, 2415 (2003).
 - [6] G. Paesold and A. O. Benz, *Astron. Astrophys.* **351**, 741 (1999).
 - [7] P. Messmer, *Astron. Astrophys.* **382**, 301 (2002).
 - [8] K. B. Quest and V. D. Shapiro, *J. Geophys. Res.* **101**, 24457 (1996).
 - [9] S. P. Gary, H. Li, S. O'Rourke, and D. Winske, *J. Geophys. Res.* **103**, 14567 (1998).
 - [10] B. J. Wang and L. N. Hau, *J. Geophys. Res.* **108**, 1463 (2003).
 - [11] J. Seough and P. H. Yoon, *J. Geophys. Res.* **117**, A08101 (2012).
 - [12] B. Abraham-Shrauner, *J. Plasma Phys.* **1**, 361 (1967).
 - [13] M. Tajiri, *J. Phys. Soc. Jpn.* **22**, 1482 (1967).
 - [14] J. F. C. Wardle, D. C. Homan, R. Ojha, and D. H. Roberts, *Nature (London)* **395**, 457 (1998).
 - [15] E. Fiandrini, G. Esposito, B. Bertucci, B. Alpat, G. Ambrosi, R. Battiston, W. J. Burger, D. Caraffini, L. Di Masso, N. Dinu, M. Ionica, R. Ionica, M. Pauluzzi, M. Menichelli, and P. Zuccon, *Space Weather* **2**, S09S02 (2004).
 - [16] E. Asseo and A. Riazuelo, *Mon. Not. R. Astron. Soc.* **318**, 983 (2000).
 - [17] M. Mościbrodzka, C. F. Gammie, J. C. Dolence, and H. Shiokawa, *Astrophys. J.* **735**, 9 (2011).
 - [18] F. A. Aharonian, S. V. Bogovalov, and D. Khangulyan, *Nature (London)* **482**, 507 (2012).
 - [19] T. Siegert, R. Diehl, J. Greiner, M. G. H. Krause, A. M. Beloborodov, M. C. Bel, F. Guglielmetti, J. Rodriguez, A. W. Strong, and X. Zhang, *Nature (London)* **531**, 341 (2016).
 - [20] C. P. Ridgers, C. S. Brady, R. Ducloux, J. G. Kirk, K. Bennett, T. D. Arber, and A. R. Bell, *Phys. Plasmas* **20**, 056701 (2013).
 - [21] G. Sarri, M. E. Dieckmann, I. Kourakis, A. Di Piazza, B. Reville, C. H. Keitel, and M. Zepf, *J. Plasma Phys.* **81**, 455810401 (2015).
 - [22] M. Vranic, O. Klimo, G. Korn, and S. Weber, *Sci. Rep.* **8**, 4702 (2018).
 - [23] R. Schlickeiser, *Open Plasma Phys. J.* **3**, 1 (2010).
 - [24] M. E. Dieckmann, D. Folini, A. Bret, and R. Walder, *Plasma Phys. Control. Fusion* **61**, 085027 (2019).
 - [25] P. Hellinger and H. Matsumoto, *J. Geophys. Res.* **105**, 10519 (2000).
 - [26] R. C. Tautz and J. I. Sakai, *Phys. Plasmas* **14**, 012104 (2007).
 - [27] C.-S. Jao and L.-N. Hau, *New J. Phys.* **17**, 053047 (2015).
 - [28] C.-S. Jao and L.-N. Hau, *Phys. Rev. E* **98**, 013203 (2018).
 - [29] L.-N. Hau and B. U. Ö. Sonnerup, *Geophys. Res. Lett.* **20**, 1763 (1993).
 - [30] L.-N. Hau, *Phys. Plasmas* **9**, 2455 (2002).
 - [31] M. Chou and L.-N. Hau, *Astrophys. J.* **611**, 1200 (2004).
 - [32] N. Iwamoto, *Phys. Rev. E* **47**, 604 (1993).
 - [33] G. P. Zank and R. G. Greaves, *Phys. Rev. E* **51**, 6079 (1995).
 - [34] Y. Omura, One-dimensional electromagnetic particle code KEMPO1: A tutorial on microphysics in space plasmas, in *Advanced Methods for Space Simulations*, edited by H. Usui and Y. Omura (TERAPUB, Tokyo, 2007).
 - [35] Y. Omura, KEMPO1 Kyoto University ElectroMagnetic Particle cOde: 1d version, in *Advanced Methods for Space Simulations*, edited by H. Usui and Y. Omura (TERAPUB, Tokyo, 2007).
 - [36] M. Lazar, S. M. Shaaban, S. Poedts, and Š. Štverák, *Mon. Not. R. Astron. Soc.* **464**, 564 (2017).
 - [37] R. A. López, M. Lazar, S. M. Shaaban, S. Poedts, P. H. Yoon, A. F. Viñas, and P. S. Moya, *Astrophys. J.* **873**, L20 (2019).